The landscape of myeloid and astrocyte phenotypes in acute multiple sclerosis lesions

Calvin Park[1], Gerald Ponath[1], Maya Levine-Ritterman[1], Edward Bull[1], Eric C. Swanson[2], Philip L. De Jager[3], Benjamin M. Segal[4], David Pitt[1]

[1] *Department of Neurology, Yale School of Medicine, New Haven, CT, USA*
[2]*Fluidigm Corporation, Markham, ON, Canada*
[3]*Department of Neurology, Columbia University Medical Center, New York, NY*
[4]*Department of Neurology, University of Michigan, Ann Arbor, MI, USA*

Author contact information
Calvin Park, Email: calvin.park@yale.edu
Gerald Ponath, Email: gerald.ponath@yale.edu
Maya Levine-Ritterman, Email: maya.levine-ritterman@yale.edu
Edward Bull, Email: embull@bowdoin.edu
Eric Swanson, Email: Eric.Swanson@fluidigm.com
Philip L. De Jager, Email: pld2115@cumc.columbia.edu
Benjamin M. Segal, Email: bmsegal@med.umich.edu

Corresponding author
David Pitt, MD
Department of Neurology
Yale School of Medicine
300 George Street, Suite 353I
New Haven, CT 06511
david.pitt@yale.edu
Phone: 203-737-7951
Fax: 203-737-2704

Abstract

Activated myeloid cells and astrocytes are the predominant cell types in active multiple sclerosis (MS) lesions. Both cell types can adopt diverse functional states that play critical roles in lesion formation and resolution. In order to identify phenotypic subsets of myeloid cells and astrocytes, we profiled acute MS lesions with thirteen glial activation markers using imaging mass cytometry (IMC), a method for multiplexed labeling of histological sections. In a demyelinating lesion, we found multiple distinct myeloid and astrocyte phenotypes that populated separate lesion zones. In a post-demyelinating lesion, phenotypes were less distinct and more uniformly distributed. In both lesions cell-to-cell interactions were not random, but occurred between specific glial subpopulations and lymphocytes. Finally, we demonstrated that myeloid, but not astrocyte phenotypes were activated along a lesion rim-to-center gradient, and that marker expression in glial cells at the lesion rim was driven more by cell-extrinsic factors than in cells at the center. This proof-of-concept study demonstrates that highly multiplexed tissue imaging, combined with the appropriate computational tools, is a powerful approach to study heterogeneity, spatial distribution and cellular interactions in the context of MS lesions. Identifying glial phenotypes and their interactions at different lesion stages may provide novel therapeutic targets for inhibiting acute demyelination and low-grade, chronic inflammation.

Keywords

Multiple Sclerosis, Imaging Mass Cytometry, Multiplexed Tissue Imaging, Single-cell Analysis, Astrocytes, Macrophages

Introduction

Multiple sclerosis (MS) is a common neurological disease, characterized by formation of inflammatory demyelinating lesions in the central nervous system (CNS) [27]. Inflammation is driven by infiltrating lymphocytes and monocytes, in concert with resident activated microglia and astrocytes. Macrophages and reactive astrocytes are the most abundant cell types in acute lesions [19,31]. These cells are highly plastic and can adopt pro-inflammatory, anti-inflammatory, neurotoxic, neuroprotective, and tissue-regenerating functions [4,6,7,21,24,30,31,43].

Previous studies have identified macrophage phenotypes in MS lesions based on the expression of single classical (M1) and alternative (M2) activation markers; however, those studies have produced limited and sometimes conflicting results [6,43]. A recent study of traumatic brain injury in mice demonstrated random expression of M1/M2 polarization markers in infiltrating macrophages in seemingly incompatible combinations [17]. This suggests that the M1/M2 polarization paradigm, which originated as an *in vitro* concept, is of limited value for distinguishing myeloid phenotypes in the inflamed CNS [36].

Current studies, including our own, are using single-cell or single-nuclear RNA sequencing to comprehensively assess the complex phenotypes of human glial cells in healthy and diseased brains [14,23,28]. Through these efforts, we and others have observed varying levels of myeloid cell/microglial diversity in the human brain depending on the neurological disease and clustering aims, where diverse functional states of microglia are associated to varying degrees with different brain pathologies. Moreover, since RNA sequencing techniques do not capture spatial information, the distribution and interactions of these subpopulations in CNS tissue have not yet been examined.

Several novel techniques make it now possible to perform high parameter imaging of histological section and evaluate complex cellular phenotypes *in situ* [5,8,9,11,42]. Imaging mass cytometry (IMC), like mass cytometry (CyTOF), relies on metal isotope-labeled antibodies and combines immunohistochemistry with high-resolution laser ablation followed by time-of-flight mass spectrometry [9,44]. This approach allows for simultaneous quantitative profiling with up to 37 antibodies on a single tissue section at subcellular resolution. Moreover, novel computational tools have become available to extract single-cell information from highly multiplexed histological data [3,25,37].

In this proof-of-concept study, we applied IMC and single-cell analytics to two active MS lesions – one demyelinating and one post-demyelinating – to examine the cellular heterogeneity of myeloid cells and astrocytes, based on thirteen markers that are known to be expressed by activated glial cells in MS lesions

[2,6,13,15,32,43,45,46]. We demonstrate that multiplexed tissue imaging, in combination with the appropriate computational tools, can extract previously unattainable information from histological sections, including definition of cellular subpopulations, their distribution within the lesion environment, specific cell-cell interactions, phenotypic transitions and the impact of spatial sources on marker expression.

Materials and methods

MS lesions.

Human CNS tissue was obtained at autopsy from two patients with relapsing-remitting MS according to Institutional Review Board-approved protocols. After autopsy, brain tissue was fixed in 10% formalin, and lesions were cut based on MRI. Lesion tissue was subsequently embedded in paraffin and sectioned at 5 μm thickness.

A highly inflamed, active lesion was chosen for analysis from each patient: the demyelinating lesion was selected from a 42-year-old male with 5 years disease duration (5.5 hour *post mortem* interval), while the post-demyelinating lesion was chosen from a 32-year-old female with 6 years disease duration (8 hour *post mortem* interval). Lesions from both patients have been characterized in previous studies [10,29].

Brightfield histology.

For basic characterization, lesions were stained against CD68, myelin basic protein (MBP) and neuronal marker MAP2, and examined with brightfield microscopy. De-paraffinized and rehydrated sections were subjected to antigen retrieval in pH 6, 10 mM citrate buffer at 96°C for 20 minutes, cooled, quenched in 0.3% peroxide, and blocked with FC receptor binding inhibitor and normal serum before incubation with primary antibody (Additional file 1: Table S1) overnight at 4°C. Sections were subsequently incubated with appropriate biotinylated secondary antibodies, processed with an avidin/biotin staining kit with 3,3-diaminobenzidene (DAB) as the chromogen (Vector ABC Elite Kit and DAB Kit, Vector Laboratories), then counterstained with hematoxylin [29]. Adequate controls using isotype control antibodies were performed for each primary antibody. Sections were rinsed with distilled water, dehydrated, and cover-slipped with Permount (Vector Laboratories). Images were acquired using a Leica DM5000 B microscope with a Leica color camera DFC310 Fx and Leica Application Suite (version 4.9.0) imaging software. Images were processed with Panoramic Viewer (3DHISTECH) and Photoshop (Adobe) software.

Antibody validation and conjugation to metal isotopes for IMC.

Several lanthanide-conjugated antibodies were purchased from Fluidigm. Antibodies not available in metal-conjugated form were purchased in carrier-free solution and validated by brightfield immunohistochemistry using the appropriate isotype control antibodies. Subsequently, antibodies were conjugated to lanthanide metal isotopes following the Maxpar® Antibody Labeling Kit protocol (Fluidigm). Metal-conjugated antibodies were stored at 0.5 mg/mL in PBS-based Antibody Stabilizer (Candor Bioscience) with 0.05% sodium azide at 4°C. Working concentrations for all metal-conjugated antibodies were optimized by IMC (Additional file 1: Table S2) on MS lesion tissue.

Imaging mass cytometry.

For IMC histology, tissue sections were de-paraffinized and rehydrated, and antigen retrieval was performed in pH 8, 1 mM EDTA buffer at 96°C for 20 minutes. Sections were cooled at room temperature and rinsed in tap water and TBS (20 mM Tris with 500 mM NaCl, pH 7.5). Tissue was blocked for 3 hours at room temperature with 0.3% BSA, 25% FBS and 0.1 mg/mL FC receptor binding inhibitor in TBS-T (TBS + 0.05% Tween-20). All antibodies (Additional file 1: Table S2) were diluted in 0.3% BSA in TBS-T and applied to the tissue for overnight incubation at 4°C. Sections were then rinsed in TBS-T and TBS, and counterstained with 125 nM Maxpar® Intercalator-Ir (Fluidigm) in PBS for 1 hour at room temperature. Sections were rinsed in TBS-T, TBS and two washes of distilled water before air-drying at room temperature. Antibody-labeled tissue areas (1000x1000 µm) were raster-ablated using a Hyperion™ Laser Scanning Module (Fluidigm) with a 1 µm diameter spot size at 200 Hz. This process was coupled to a Helios™ Mass Cytometer (Fluidigm) for lanthanide metal detection [44]. Images for each antibody channel were acquired on CyTOF Software (Fluidigm, version 6.7). MCD Viewer (Fluidigm, version 1.0) was used to export raw 16-bit tiff images for computational analyses on histoCAT (version 1.75) [37]. For visualization purposes, images were processed in MCD Viewer and ImageJ [39].

Computational analyses.

Single-cell segmentation. Merged CD68 (macrophages/microglia), S100B (astrocytes), and CD3 (T cells) antibody channel images were used to segment single cell objects on CellProfiler (version 3.0.0) [16]. The resulting segmentation mask images, which outline cell borders, were loaded into histoCAT with corresponding antibody channel images.

Identification of cellular phenotypes. Mean single-cell marker intensity values were extracted from segmented antibody channel images on histoCAT and Z-score normalized. Based on the expression intensities of thirteen markers (Additional file 1: Table S2), cell clusters were defined using the PhenoGraph algorithm [20] integrated into histoCAT. Default parameters with 75 nearest neighbors for the early lesion and 50 nearest neighbors for the late lesion were used. These nearest neighbor values were chosen such that over- and under-clustering of phenotypes were avoided. Additional normalization steps were performed internally, as previously described [37].

Analysis of cellular phenotypes. To visualize clusters, the Barnes-Hut t-SNE algorithm implemented in histoCAT was executed with the same image and marker inputs used in PhenoGraph, as well as default parameters (initial dimensions, 110; perplexity, 30; theta, 0.5) and internal normalization [1,37]. t-SNE plots were colored to highlight cell clusters or lesion samples, or to show relative marker expression intensity. Images of cell phenotypes visualized in the tissue, as well as segmentation masks overlaid with histology images, were generated in histoCAT. For the remaining analyses, ".csv" files containing single-cell parameters were exported from histoCAT and appropriately processed for their application. To produce an expression heatmap for clusters, normalized marker intensity values were processed using the R *ComplexHeatmap* package, which hierarchically clusters single cells within clusters using Ward's method [38]. Violin plots showing single-cell marker expression variability for each cluster were generated using the R *ggplot2* package [12]. To study phenotype transitions, Potential of Heat-diffusion Affinity-based Transition Embedding (PHATE) mapping and Monocle Pseudotime analyses were performed [25,34,35,41]. PHATE mapping was performed using normalized marker intensity values, with an adjusted number of nearest neighbors ($k = 100$) and other parameters left as their default specifications. Pseudotime analysis was performed with negative binomial normalization of marker intensity values and $q < 1$ to incorporate all markers, based on a test for differential expression among phenotypes. Figures showing phenotype cell size and relative quantity of cells per cluster, as well as correlation matrices and corresponding marker scatter plots with linear regression lines were produced in Prism (version 7). FlowJo software (version 10.5.3) was used to visualize single-cell marker data on flow cytometry plots. Images and figures were recolored when necessary in Photoshop.

Analysis of cell spatial relationships. To study the spatial relationships of cell clusters, neighborhood analysis was performed on histoCAT using the PhenoGraph-generated clusters pertaining to each lesion. Significant pairwise phenotype interactions and avoidances were determined by an unbiased permutation test which compared the frequency of one cell type neighboring another to the frequency in 999 random permutations of cell cluster labels.

Neighbors were identified within 4 μm from each cell, and neighboring frequency was normalized to the number of interacting cells [37]. Analyses were performed for different degrees of significance ($p < 0.05$ and $p < 0.01$), and the results were reported on a heatmap. To identify sources of single-cell marker variation, spatial variance component analysis (SVCA) [3] was performed on Python for different lesion zones, using standardized marker intensity values. SVCA plots were generated in R and Prism.

Statistical analyses. In plots showing phenotype cell size, data represent mean cell areas + standard deviation. Comparisons of phenotype cell sizes were analyzed by one-way ANOVA followed by the Tukey-Kramer multiple comparison test. Comparisons of two samples were carried out by unpaired Student's t-tests. For correlation analyses, Pearson correlation coefficients were computed. $*p < 0.0001$.

Results

Histology and cell clustering overview

We analyzed one demyelinating and one post-demyelinating MS lesion according to a classification by Kuhlmann et al. [18], referred to throughout this report as the "early" and "late" lesion, respectively. Both lesions were located in the brain stem and characterized by complete loss of myelin, hypercellularity with the highest cellular density at the lesion rim, and diffuse infiltration with foamy macrophages. The laser-scanned area of the early lesion involved predominantly white matter (WM) but also interspersed gray matter (G/WM), while the scanned area of the late lesion consisted of only WM (Fig. 1).

Consistent with demyelinating activity, macrophages at the rim of the early lesion contained myelin basic protein (MBP)-positive myelin debris, which was absent in macrophages from the late lesion (Fig. 1d, j) [18]. Moreover, foamy macrophages were numerous and large in size in the rim of the early lesion, whereas macrophages in the rim of the late lesion were smaller and less concentrated (Fig. 1e, k).

Perivascular infiltrates in the early lesion contained mostly lymphocytes and only a few undifferentiated monocytes, while the perivascular cuffs in the late lesion consisted predominantly of lipid-laden macrophages, as described previously (Fig. 1i, l) [22,40]. We defined single cells by segmenting cell bodies outlined by the markers CD68 (macrophages/microglia), S100B (astrocytes), and CD3 (T cells) using CellProfiler (Additional file 1: Figure S1) [16]. This allowed for a clear delineation of cell types in the vast majority of cells. In a small fraction of cells, we found overlap between cellular markers, especially between myelin fibers and juxtaposed microglial processes in

normal-appearing white matter (NAWM), and between astrocyte processes and closely neighboring macrophages (Additional file 1: Figure S1c, d). We did not exclude these cells in order to avoid bias in our spatial analysis. However, we excluded perivascular lymphocytes from the early lesion, as they were too densely packed to be identifiable as individual cells.

Segmentation masks were overlaid with corresponding images from thirteen antibody channels (Additional file 1: Figures S2, S3) in histoCAT [37], which clustered myeloid cells and astrocytes into phenotypic subpopulations based on their marker expression profiles. The optimal number of phenotype clusters was determined based on separation of the principal cell types (i.e. myeloid cells, astrocytes and T cells) and distinctive expression profiles of phenotypes, using expression heatmaps and t-SNE plots. This resulted in a total of twelve phenotypes for each lesion (Figs. 2, 4).

Phenotype heterogeneity and distribution in early demyelination

In the early lesion, we analyzed a total of 4,397 cells, of which 66.3% were myeloid cells and 32.5% were astrocytes (Additional file 1: Figure S4a). This ratio was higher at the rim than the lesion center. The cells clustered into six myeloid and five astrocyte subtypes (Fig. 2). The myeloid phenotypes were spatially sequestered in four lesional regions, i.e. NAWM, outer lesion rim, inner lesion rim, and center. Within the outer lesion rim, we observed one myeloid cell phenotype at the G/WM interface (m1) and two phenotypes located in the WM rim (m4, m5). The other lesion areas were all occupied by one myeloid phenotype (Fig. 3a). Most myeloid cell activation markers were highly expressed in the outer lesion rim and decreased in intensity towards the lesion center (Fig. 2a, b). The m1 phenotype at the G/WM interface showed the highest activation profile. m5 cells in the outer WM rim were the largest in size, whereas m2 cells in the lesion center were the smallest (Additional file 1: Figure S4b); this may reflect the amount of myelin fragments phagocytosed by foamy macrophages at the advancing lesion edge, and the degradation of myelin in phagocytes within the lesion center [33].

Astrocyte phenotypes were each defined by one distinct, highly expressed marker (Fig. 2a, b). Analogous to the myeloid phenotypes, the five astrocyte phenotypes were also spatially stratified into the NAWM, lesion rim, and lesion center (Fig. 3b). Furthermore, a5 astrocytes located in the outer rim within WM were larger than all other phenotypes (Additional file 1: Figure S4b). Unlike in myeloid cells, marker expression in astrocytes did not follow a gradient from the rim to the lesion center, but was uniform throughout the lesion.

T cells made up the smallest population of all immune infiltrates, and were concentrated within the lesion center (Fig. 3c; Additional file 1: Figure S4a). These cells uniformly expressed CD45 and HLA-DR (Fig. 2a, b), and did not separate into different clusters.

To determine possible transitions between phenotypes, we applied Potential of Heat-diffusion Affinity-based Transition Embedding (PHATE) mapping and Pseudotime to the myeloid cell and astrocyte populations. PHATE mapping improves on t-SNE by better visualizing phenotype transitions, where smooth continua from one phenotype to another indicate a transition trajectory [25]. Rather than a rim-to-center continuum that aligned with the sequential organization of phenotypes in the lesion, our analysis showed only a partial continuum between the G/WM outer rim phenotype (m1) and the lesion center phenotype (m2) (Fig. 3d), without including the inner rim phenotype (m3). Similarly, analysis with Pseudotime, an alternative tool for visualizing phenotype transitions [41], showed that myeloid phenotypes did not follow a linear transition trajectory but branched into several independent fates (Fig. 3e). PHATE mapping and Pseudotime analysis of astrocyte phenotypes also suggested independent phenotypic fates rather than linear phenotype trajectories (Additional file 1: Figure S5a, Pseudotime analysis not shown).

Low phenotype heterogeneity and random phenotype distributions in the late demyelinating lesion

In the late, post-demyelinating lesion we analyzed 6,698 cells, with myeloid cells far outnumbering astrocytes (91.1% myeloid cells; Additional file 1: Figure S6a), particularly at the lesion rim. The same clustering criteria used for the early lesion resulted in nine myeloid phenotypes and two astrocyte phenotypes in this late lesion (Fig. 4). Myeloid phenotypes separated into lesion rim (m3), perivascular space (m4), and NAWM (m7) zones (Fig. 5a). In contrast to the early lesion, the other six myeloid phenotypes were intermixed throughout the lesion center. These phenotypes showed a low degree of separation on the t-SNE plot, indicating similar marker expression profiles (Fig. 4c). The phenotypes in the lesion rim and the perivascular space (m3, m4) were characterized by high expression of the majority of markers, and shared a similar expression profile with the G/WM rim phenotype in the early lesion (m1) (Fig. 4a, b). As in the early lesion, myeloid phenotypes in the lesion rim (m3) and perivascular space (m4) were significantly larger than those in the lesion center (Additional file 1: Figure S6b), but were overall smaller than in the early lesion (data not shown).

Astrocytes were clustered into two phenotypes, with one phenotype localizing primarily to the lesion rim, and the other to the lesion center (Fig. 5b). The rim phenotype (a2) exhibited a marker expression profile similar to the rim phenotype in the early lesion (a5), (Fig. 4a, b). Finally, T cells were few (Fig. 5c; Additional file 1: Figure S6a), and expressed the activation markers CD45 and HLA-DR (Fig. 4a, b), as observed in the early lesion. To directly compare cell populations in both lesions, we mapped cells from both lesions on the same t-SNE plot. Cell populations overlapped only moderately, highlighting the differences between the phenotypes from each lesion (Additional file 1: Figure S7).

PHATE mapping demonstrated a partial continuum between two lesion center myeloid phenotypes (m2, m6) and the perivascular space phenotype (m4) (Fig. 5d), which was confirmed by Pseudotime (Fig. 5e). These analyses support a lesion center-to-perivascular transition, but not a continuum where all phenotypes align along a rim-to-center transition axis. The same analyses for astrocytes showed substantial overlap between both phenotypes but not a linear transition (Additional file 1: Figure S5b, Pseudotime analysis not shown).

In the early lesion, we found no correlation between the expression intensities of different markers at a single-cell level (Additional file 1: Figure S8a, b). This was true for an analysis of all cells and cells of each phenotype (data not shown). In the late lesion, we found strong correlations between the M2 markers MerTK and Mac2, and MerTK and LAMP1 in both myeloid cells and astrocytes (Additional file 1: Figure S8c, d). This resulted from high and continuous dynamic ranges of marker expression (Fig. 6). Correlations were weak between the other marker pairs.

Phenotypes in the early and late acute lesions engaged in specific cell-cell interactions

We next investigated the spatial relationships between different phenotypes with a computational tool integrated into histoCAT that performs an unbiased, systematic analysis of pairwise phenotype interactions and avoidances [37]. After excluding interactions between cells of the same or spatially adjacent phenotypes, our analysis demonstrated distinct interaction signatures for both lesions, (Fig. 7a, b). At a significance cut-off of $p < 0.01$, these included interactions between inner rim myeloid phenotype m3 (MerTK and CD45 high) and astrocyte phenotype a1 (Mac2 high), as well as interaction of highly activated myeloid rim phenotype m1 and the rim/center phenotype m4 (HLA-DR and ferritin high) with astrocyte phenotype a2 (HLA-DR high) in the early lesion. In the late lesion, highly activated perivascular macrophages (m4) interacted with most myeloid cell phenotypes and both astrocyte phenotypes. There were also significant interactions between myeloid and astrocyte phenotypes m6 and a1, and

among lesion center myeloid phenotypes (m6 with m7 and m8). At a significance cut-off of $p < 0.05$, we found that T cells in the late lesion interacted with myeloid phenotypes in the perivascular space (m4), which expressed HLA-DR, and in the lesion center (m8).

Influence of lesion environment on marker expression

Finally, we used spatial variance component analysis (SVCA) to model the effects of extrinsic factors (neighboring cells and non-cellular environmental stimuli) and cell-intrinsic factors on variations in cell marker expression [3]. In the rim of both lesions, the expression of several markers was highly influenced by neighboring cells, including CD86, PLP, and Mac2 in the early lesion, and CD86, PLP and LAMP1 in the late lesion. Other markers, such as ferritin, vimentin, and CD3 (early lesion), and ferritin, vimentin, and TIM-3 (late lesion), were driven predominantly by non-cellular environmental stimuli (Fig. 7c, d). The relative influence of these factors changed toward the inner lesion rim and center, leading to an overall increased impact of cell-intrinsic factors and a decrease in the influence of external factors. In the lesion center, the primary agents influencing marker expression were cell-intrinsic factors and, to a lower degree, environmental stimuli (Fig. 7c, d).

Discussion

Our study examines the landscape of myeloid and astrocyte phenotypes in early and late acute MS brain lesions using IMC. To our knowledge, this is the first application of highly multiplexed imaging to MS tissue. We applied thirteen markers that are known to be expressed by activated glial cells during MS lesion development. Clustering resulted in eleven myeloid cell and astrocyte phenotypes that localized to distinct lesion areas. Moreover, individual phenotypes interacted selectively with other cell types, and marker expression was driven by different factors in cells within the lesion rim than the center. Thus, our approach provides a wealth of data on cellular spatial organization that is not accessible with standard histology.

The alignment of myeloid cell phenotypes with different lesional layers suggests functional specificity and validates our clustering approach. This spatial separation was most pronounced in the early lesion, but was lost in the center of the late lesion, where phenotypes were intermixed. In addition, marker expression was the highest in myeloid phenotypes located at the lesion rim and diminished substantially towards the lesion center in both lesions. Consistent with the different stages of myelin phagocytosis and degradation, the myeloid phenotypes in the rim were larger than those in the lesion center. An additional feature of the late lesion was the presence of numerous, highly

activated macrophages in perivascular spaces throughout the lesion. Since these macrophages are believed to transition into the vasculature [22], this may indicate they exit the CNS in a highly activated state. In contrast to myeloid cells, marker expression in astrocyte phenotypes did not follow a rim-to-center gradient, but was comparable throughout the lesion.

Using PHATE mapping and Pseudotime to determine transitions between phenotypes, we found that myeloid cell or astrocyte phenotypes did not develop along a linear transition continuum, e.g. from the outer to the inner lesion rim and lesion center. Instead, the different phenotypes branched into multiple independent trajectories, suggesting that they emerge within the lesion environment independent from each other. We cannot exclude that the parametric depth of our study is too low to detect transition states, especially since Pseudotime has been developed to delineate phenotypic trajectories from whole transcriptome sequencing data [41].

Neighborhood analysis demonstrated distinct cellular interaction signatures for both lesions, e.g. between phagocytic inner rim macrophages and center astrocytes in the early lesion, and between T cells and two myeloid phenotypes in the late lesion. This indicates that cellular interactions are not random in this hypercellular lesion environment, but occur between specific subpopulations and cell types such as lymphocytes. The low parametric depth of our study does not allow us to identify the functional implications of these interactions; however, they may represent nodal points of cellular communication critical for lesion formation and maintenance of low-grade inflammation.

Finally, spatial variance component analysis (SVCA) suggests that cell-extrinsic factors drive marker expression to a higher degree in the lesion rim than in the center. Conversely, cell-intrinsic factors have a more prominent influence on marker expression in the lesion center. This suggests that glia cells in the lesion rim respond more to cues from the microenvironment, such as cytokines or receptor-ligand interactions, while glial activation in the lesion center is the result of cell-intrinsic programs such as cellular changes set in motion by myelin phagocytosis.

Myeloid cell/microglial heterogeneity has recently been examined by us and others with single-cell RNA sequencing in healthy CNS, MS lesions and neurological diseases such as Alzheimer's disease, Parkinson's disease and temporal lobe epilepsy [23,28]. In keeping with our results, these efforts have identified multiple myeloid cell/microglial phenotypes; specifically, Masuda and colleagues determined nine myeloid cell phenotypes in MS lesions and healthy brain [23], and we found ten myeloid phenotypes across multiple neurodegenerative diseases [28]. In the latter study, we identified one microglia cluster (cluster 7), characterized by high expression of CD74,

which was enriched for genes associated with MS susceptibility. This cluster was the most congruent with our rim phenotypes, as it was enriched for several genes that were highly expressed at the rim of our lesions, i.e. LAMP1, CD45, CD68, CD86 and HLA-DR. Moreover, we confirmed that this cluster localized to the lesion by staining our lesions for CD74 (data not shown). Other attempts to cluster myeloid cells in experimental autoimmune encephalomyelitis (EAE), a mouse model of MS, using single-cell cytometry [26], and in MS lesions using single nuclear RNA sequencing [14], have yielded substantially less myeloid cell heterogeneity.

Our study is limited by the small sample size and the low number of markers, which may result in inaccurate phenotype clustering. However, as a proof-of-concept study, it demonstrates the ability of multiplexed tissue imaging and appropriate single-cell analytics to reveal the heterogeneity and spatial properties of glial cell phenotypes in MS lesions.

Conclusions

In summary, we found that phenotypic clustering based on differential expression of thirteen glial activation markers produced multiple myeloid cell and astrocyte phenotypes that occupied specific lesion zones. Myeloid cells were activated along a rim-to-center axis, and specific myeloid cell-astrocyte-lymphocyte interactions were present in both lesions. Our study highlights the potential of imaging mass cytometry, paired with novel computational tools, to provide insight into lesion-forming phenotypes and their spatial organization in MS lesions.

In ongoing studies, we are combining cell clustering based on single-nuclear RNA sequencing data of MS lesion-derived glial cells with highly multiplexed imaging to simultaneously obtain maximal parametric depth and high spatial resolution at single-cell level. The results will help define the phenotypes and key interaction networks that drive active demyelination and chronic, low-grade inflammation in established lesions and may ultimately provide targets for therapeutic intervention in relapsing and progressive MS.

List of abbreviations

MS: multiple sclerosis

CNS: central nervous system

IMC: imaging mass cytometry

CyTOF: mass cytometryMBP: myelin basic protein

DAB: 3,3-diaminobenzidene

PHATE: Potential of Heat-diffusion Affinity-based Transition Embedding

SVCA: spatial variance component analysis

WM: white matter

G/WM: gray and white matter

NAWM: normal-appearing white matterG/WMoR: gray and white matter outer rim

WMoR: white matter outer rim

iR: inner rim

WM R/C: white matter rim/center

C: center

R: rim

PVS: perivascular space

EAE: experimental autoimmune encephalomyelitis

Additional file

Additional file 1 (DOCX): Tables S1-S2 and Figures S1-S8.

Declarations

Ethics approval and consent to participate

Full ethical approval for the use of de-identified, human CNS autopsy tissue was obtained according to Institutional Review Board-approved protocols (Yale Human Investigation Committee), and informed consent was received from all human participants.

Consent for publication

Not applicable.

Availability of data and materials

The datasets generated and/or analyzed during the current study as well as R code are available in a GitHub repository, https://github.com/PittLab/IMC_Park_et_al_2019.

Competing interests

The authors declare no competing interests.

Funding

D.P. is supported by the by the National Institutes of Health grants R01 NS102267 and R01 NS10538502. B.M.S. is supported by the National Institutes of Health grants R01 NS10538502. P.L.D. is supported by NMSS planning grant R-1810-32681. The funding bodies had no part in the design of the study and collection, analysis, and interpretation of data or in writing the manuscript.

Authors' contributions

D.P., C.P. and G.P. conceived and designed the study; C.P. performed the experiments; C.P., G.P. and D.P. analyzed the data; G.P., M.L.-R., E.B., E.C.S., P.L.D., B.M.S. and D.P. provided methodological, technical and/or scientific assistance; E.C.S. provided IMC tissue imaging service; C.P., G.P., M.L.-R., E.C.S., P.L.D., B.M.S. and D.P. reviewed the manuscript; C.P. and D.P. wrote the manuscript.

Acknowledgments

The authors thank Fluidigm Corporation (Markham, ON, Canada) and the Yale University CyTOF core facility for providing IMC tissue imaging service and metal-conjugated antibodies, as well as Denis Schapiro, Damien Arnol and Kevin Moon for expert assistance with computational analyses.

References

1. Amir E-aD, Davis KL, Tadmor MD, Simonds EF, Levine JH, Bendall SC, Shenfeld DK, Krishnaswamy S, Nolan GP, Pe'er D (2013) viSNE enables visualization of high dimensional single-cell data and reveals phenotypic heterogeneity of leukemia. Nature Biotechnology 31:545. doi:10.1038/nbt.2594
2. Anderson AC, Anderson DE, Bregoli L, Hastings WD, Kassam N, Lei C, Chandwaskar R, Karman J, Su EW, Hirashima M, Bruce JN, Kane LP, Kuchroo VK, Hafler DA (2007) Promotion of tissue inflammation by the immune receptor Tim-3 expressed on innate immune cells. Science 318:1141-1143. doi:10.1126/science.1148536
3. Arnol D, Schapiro D, Bodenmiller B, Saez-Rodriguez J, Stegle O (2018) Modelling cell-cell interactions from spatial molecular data with spatial variance component analysis. bioRxiv:265256. doi:10.1101/265256
4. Bartnik BL, Juurlink BH, Devon RM (2000) Macrophages: their myelinotrophic or neurotoxic actions depend upon tissue oxidative stress. Multiple sclerosis (Houndmills, Basingstoke, England) 6:37-42. doi:10.1177/135245850000600108
5. Bolognesi MM, Manzoni M, Scalia CR, Zannella S, Bosisio FM, Faretta M, Cattoretti G (2017) Multiplex Staining by Sequential Immunostaining and Antibody Removal on Routine Tissue Sections. The journal of histochemistry and cytochemistry : official journal of the Histochemistry Society 65:431-444. doi:10.1369/0022155417719419
6. Boven LA, Van Meurs M, Van Zwam M, Wierenga-Wolf A, Hintzen RQ, Boot RG, Aerts JM, Amor S, Nieuwenhuis EE, Laman JD (2006) Myelin-laden macrophages are anti-inflammatory, consistent with foam cells in multiple sclerosis. Brain : a journal of neurology 129:517-526. doi:10.1093/brain/awh707
7. Farina C, Aloisi F, Meinl E (2007) Astrocytes are active players in cerebral innate immunity. Trends in immunology 28:138-145. doi:10.1016/j.it.2007.01.005
8. Gerner Michael Y, Kastenmuller W, Ifrim I, Kabat J, Germain Ronald N (2012) Histo-Cytometry: A Method for Highly Multiplex Quantitative Tissue Imaging Analysis Applied to Dendritic Cell Subset Microanatomy in Lymph Nodes. Immunity 37:364-376. doi:https://doi.org/10.1016/j.immuni.2012.07.011
9. Giesen C, Wang HAO, Schapiro D, Zivanovic N, Jacobs A, Hattendorf B, Schüffler PJ, Grolimund D, Buhmann JM, Brandt S, Varga Z, Wild PJ, Günther D, Bodenmiller B (2014) Highly multiplexed imaging of tumor tissues with subcellular resolution by mass cytometry. Nature methods 11:417. doi:10.1038/nmeth.2869
10. Giles DA, Washnock-Schmid JM, Duncker PC, Dahlawi S, Ponath G, Pitt D, Segal BM (2018) Myeloid cell plasticity in the evolution of central nervous system autoimmunity. Annals of neurology 83:131-141. doi:10.1002/ana.25128
11. Gut G, Herrmann MD, Pelkmans L (2018) Multiplexed protein maps link subcellular organization to cellular states. Science 361:eaar7042. doi:10.1126/science.aar7042
12. Hadley W (2016) ggplot2: Elegant Graphics for Data Analysis. Springer-Verlag New York,
13. Hametner S, Wimmer I, Haider L, Pfeifenbring S, Bruck W, Lassmann H (2013) Iron and neurodegeneration in the multiple sclerosis brain. Ann Neurol 74:848-861. doi:10.1002/ana.23974
14. Jakel S, Agirre E, Mendanha Falcao A, van Bruggen D, Lee KW, Knuesel I, Malhotra D, Ffrench-Constant C, Williams A, Castelo-Branco G (2019) Altered human oligodendrocyte heterogeneity in multiple sclerosis. Nature 566:543-547. doi:10.1038/s41586-019-0903-2
15. Kalyvas A, Baskakis C, Magrioti V, Constantinou-Kokotou V, Stephens D, López-Vales R, Lu J-Q, Yong VW, Dennis EA, Kokotos G, David S (2009) Differing roles for members of the phospholipase A2 superfamily in experimental autoimmune encephalomyelitis. Brain : a journal of neurology 132:1221-1235. doi:10.1093/brain/awp002
16. Kamentsky L, Jones TR, Fraser A, Bray MA, Logan DJ, Madden KL, Ljosa V, Rueden C, Eliceiri KW, Carpenter AE (2011) Improved structure, function and compatibility for CellProfiler: modular high-throughput image analysis software. Bioinformatics (Oxford, England) 27:1179-1180. doi:10.1093/bioinformatics/btr095
17. Kim CC, Nakamura MC, Hsieh CL (2016) Brain trauma elicits non-canonical macrophage activation states. J Neuroinflammation 13:117. doi:10.1186/s12974-016-0581-z
18. Kuhlmann T, Ludwin S, Prat A, Antel J, Brück W, Lassmann H (2017) An updated histological classification system for multiple sclerosis lesions. Acta Neuropathologica 133:13-24. doi:10.1007/s00401-016-1653-y
19. Lassmann H (2018) Multiple Sclerosis Pathology. Cold Spring Harbor perspectives in medicine 8. doi:10.1101/cshperspect.a028936
20. Levine JH, Simonds EF, Bendall SC, Davis KL, Amir el AD, Tadmor MD, Litvin O, Fienberg HG, Jager A, Zunder ER, Finck R, Gedman AL, Radtke I, Downing JR, Pe'er D, Nolan GP (2015) Data-Driven

Phenotypic Dissection of AML Reveals Progenitor-like Cells that Correlate with Prognosis. Cell 162:184-197. doi:10.1016/j.cell.2015.05.047

21. Liddelow SA, Guttenplan KA, Clarke LE, Bennett FC, Bohlen CJ, Schirmer L, Bennett ML, Münch AE, Chung W-S, Peterson TC, Wilton DK, Frouin A, Napier BA, Panicker N, Kumar M, Buckwalter MS, Rowitch DH, Dawson VL, Dawson TM, Stevens B, Barres BA (2017) Neurotoxic reactive astrocytes are induced by activated microglia. Nature 541:481. doi:10.1038/nature21029
22. Love S, Louis D, Ellison DW, Sobel RA, Moore GRW (2008) Chapter 20: Demyelinating diseases. In: Greenfield's Neuropathology. Boca Raton, FL: CRC Press; p. 1526.
23. Masuda T, Sankowski R, Staszewski O, Böttcher C, Amann L, Sagar, Scheiwe C, Nessler S, Kunz P, van Loo G, Coenen VA, Reinacher PC, Michel A, Sure U, Gold R, Grün D, Priller J, Stadelmann C, Prinz M (2019) Spatial and temporal heterogeneity of mouse and human microglia at single-cell resolution. Nature 566:388-392. doi:10.1038/s41586-019-0924-x
24. Mayo L, Trauger SA, Blain M, Nadeau M, Patel B, Alvarez JI, Mascanfroni ID, Yeste A, Kivisakk P, Kallas K, Ellezam B, Bakshi R, Prat A, Antel JP, Weiner HL, Quintana FJ (2014) Regulation of astrocyte activation by glycolipids drives chronic CNS inflammation. Nature medicine 20:1147-1156. doi:10.1038/nm.3681
25. Moon KR, van Dijk D, Wang Z, Gigante S, Burkhardt D, Chen W, van den Elzen A, Hirn MJ, Coifman RR, Ivanova NB, Wolf G, Krishnaswamy S (2018) Visualizing Transitions and Structure for Biological Data Exploration. bioRxiv:120378. doi:10.1101/120378
26. Mrdjen D, Pavlovic A, Hartmann FJ, Schreiner B, Utz SG, Leung BP, Lelios I, Heppner FL, Kipnis J, Merkler D, Greter M, Becher B (2018) High-Dimensional Single-Cell Mapping of Central Nervous System Immune Cells Reveals Distinct Myeloid Subsets in Health, Aging, and Disease. Immunity 48:380-395.e386. doi:10.1016/j.immuni.2018.01.011
27. Nylander A, Hafler DA (2012) Multiple sclerosis. The Journal of clinical investigation 122:1180-1188. doi:10.1172/jci58649
28. Olah M, Menon V, Habib N, Taga M, Yung C, Cimpean M, Khairalla A, Dionne D, Hopp S, Frosch MP, Hyman BT, Beach T, Sarkis R, Cosgrove GR, Helgager J, Golden JA, Pennell PB, Schneider JA, Bennett DA, Regev A, Elyaman W, Bradshaw EM, De Jager PL (2018) A single cell-based atlas of human microglial states reveals associations with neurological disorders and histopathological features of the aging brain. bioRxiv:343780. doi:10.1101/343780
29. Pitt D, Nagelmeier IE, Wilson HC, Raine CS (2003) Glutamate uptake by oligodendrocytes: Implications for excitotoxicity in multiple sclerosis. Neurology 61:1113-1120
30. Ponath G, Lincoln MR, Levine-Ritterman M, Park C, Dahlawi S, Mubarak M, Sumida T, Airas L, Zhang S, Isitan C, Nguyen TD, Raine CS, Hafler DA, Pitt D (2018) Enhanced astrocyte responses are driven by a genetic risk allele associated with multiple sclerosis. Nature Communications 9:5337. doi:10.1038/s41467-018-07785-8
31. Ponath G, Park C, Pitt D (2018) The Role of Astrocytes in Multiple Sclerosis. Frontiers in immunology 9:217-217. doi:10.3389/fimmu.2018.00217
32. Ponath G, Ramanan S, Mubarak M, Housley W, Lee S, Sahinkaya FR, Vortmeyer A, Raine CS, Pitt D (2016) Myelin phagocytosis by astrocytes after myelin damage promotes lesion pathology. Brain : a journal of neurology 140:399-413. doi:10.1093/brain/aww298
33. Prineas J (1975) Pathology of the early lesion in multiple sclerosis. Human pathology 6:531-554
34. Qiu X, Hill A, Packer J, Lin D, Ma YA, Trapnell C (2017) Single-cell mRNA quantification and differential analysis with Census. Nature methods 14:309-315. doi:10.1038/nmeth.4150
35. Qiu X, Mao Q, Tang Y, Wang L, Chawla R, Pliner HA, Trapnell C (2017) Reversed graph embedding resolves complex single-cell trajectories. Nature methods 14:979-982. doi:10.1038/nmeth.4402
36. Ransohoff RM (2016) A polarizing question: do M1 and M2 microglia exist? Nature neuroscience 19:987. doi:10.1038/nn.4338
37. Schapiro D, Jackson HW, Raghuraman S, Fischer JR, Zanotelli VRT, Schulz D, Giesen C, Catena R, Varga Z, Bodenmiller B (2017) histoCAT: analysis of cell phenotypes and interactions in multiplex image cytometry data. Nature methods 14:873-876. doi:10.1038/nmeth.4391
38. Schlesner M, Gu Z, Eils R (2016) Complex heatmaps reveal patterns and correlations in multidimensional genomic data. Bioinformatics (Oxford, England) 32:2847-2849. doi:10.1093/bioinformatics/btw313
39. Schneider CA, Rasband WS, Eliceiri KW (2012) NIH Image to ImageJ: 25 years of image analysis. Nature methods 9:671-675
40. Tanaka R, Iwasaki Y, Koprowski H (1975) Ultrastructural studies of perivascular cuffing cells in multiple sclerosis brain. The American journal of pathology 81:467-478

41. Trapnell C, Cacchiarelli D, Grimsby J, Pokharel P, Li S, Morse M, Lennon NJ, Livak KJ, Mikkelsen TS, Rinn JL (2014) The dynamics and regulators of cell fate decisions are revealed by pseudotemporal ordering of single cells. Nat Biotechnol 32:381-386. doi:10.1038/nbt.2859

42. Tsujikawa T, Kumar S, Borkar RN, Azimi V, Thibault G, Chang YH, Balter A, Kawashima R, Choe G, Sauer D, El Rassi E, Clayburgh DR, Kulesz-Martin MF, Lutz ER, Zheng L, Jaffee EM, Leyshock P, Margolin AA, Mori M, Gray JW, Flint PW, Coussens LM (2017) Quantitative Multiplex Immunohistochemistry Reveals Myeloid-Inflamed Tumor-Immune Complexity Associated with Poor Prognosis. Cell reports 19:203-217. doi:10.1016/j.celrep.2017.03.037

43. Vogel DYS, Vereyken EJF, Glim JE, Heijnen PDAM, Moeton M, van der Valk P, Amor S, Teunissen CE, van Horssen J, Dijkstra CD (2013) Macrophages in inflammatory multiple sclerosis lesions have an intermediate activation status. Journal of neuroinflammation 10:35-35. doi:10.1186/1742-2094-10-35

44. Wang HA, Grolimund D, Giesen C, Borca CN, Shaw-Stewart JR, Bodenmiller B, Gunther D (2013) Fast chemical imaging at high spatial resolution by laser ablation inductively coupled plasma mass spectrometry. Analytical chemistry 85:10107-10116. doi:10.1021/ac400996x

45. Weinger JG, Omari KM, Marsden K, Raine CS, Shafit-Zagardo B (2009) Up-regulation of soluble Axl and Mer receptor tyrosine kinases negatively correlates with Gas6 in established multiple sclerosis lesions. The American journal of pathology 175:283-293. doi:10.2353/ajpath.2009.080807

46. Yamada T, Kawamata T, Walker DG, McGeer PL (1992) Vimentin immunoreactivity in normal and pathological human brain tissue. Acta Neuropathologica 84:157-162. doi:10.1007/BF00311389

Figure legends

Fig. 1 Brightfield images of the MS lesions examined with IMC. **(a-f, i)** Staining of the early, actively demyelinating lesion for **(a)** myelin basic protein (MBP), **(b)** CD68 (macrophages/microglia) and **(c)** the neuronal marker MAP2. The black rectangle in **(a)** shows the region that was laser-ablated for IMC, capturing the NAWM, hypercellular rim on both sides and lesion center. Red boxes in **a-c** correspond to magnified rim areas in **d-f,** demonstrating in **(d)** condensed myelin fragments, indicative of ongoing demyelination, **(e)** dense infiltration with foamy macrophages and **(f)** dispersed neuronal cell bodies in the right lesion rim.
(g, h, j-l) Staining against MBP and CD68 in the late, post-demyelinating lesion. The black rectangle in **(g)** shows the region laser-ablated for IMC. **(j, k)** Details from **(g)** and **(h)** showing absence of myelin fragments and reduced myeloid cell density at the lesion rim compared to **(e)**. $CD68^+$ cells in the perivascular spaces of **(i)** the early lesion and **(l)** the late lesion. Images show hematoxylin counterstaining. Scale bars **a-c, g, h** = 500 μm. Scale bars **d-f, i, j-l** = 25 μm

Fig. 2 Early lesion cell phenotype profiles. **(a)** Marker expression heatmap for the myeloid, astrocyte and T cell phenotypes, identified by PhenoGraph clustering on histoCAT using segmented cells (n = 4397). The heatmap displays relative expression levels based on Z-score normalized marker intensity values, and single cells are hierarchically clustered within each phenotype group. Labels at the bottom of the heatmap indicate the area of the lesion to which each phenotype localizes. **(b)** Violin plot representation of the data in **(a)**. **(c)** t-SNE plot showing the distinct phenotype clusters. **(d)** t-SNE plot colored by marker intensity, confirming the separation of $CD68^+$, $S100B^+$ and $CD3^+$ cell types. G/WMoR = gray and white matter outer rim; WMoR = white matter outer rim; iR = inner rim; WM R/C = white matter rim/center; C = center; NAWM = normal-appearing white matter

Fig. 3 Early lesion phenotype spatial distributions and transition analyses. **(a, b)** Spatial separation of **(a)** myeloid cell and **(b)** astrocyte phenotypes into NAWM, rim and center lesion zones. **(c)** T cells are primarily located in the lesion center. **(d)** PHATE mapping of myeloid cells, indicating that the G/WM outer rim (m1) and lesion center phenotypes (m2) are on a transition continuum (white arrow). **(e)** Pseudotime analysis of myeloid cells shows that phenotypes transition along independent trajectories. Phenotype color schemes on the PHATE and Pseudotime plots reflect the color palettes specific to each analysis. Scale bar for **a-c** = 200 μm. G/WMoR = gray and white matter outer rim; WMoR = white matter outer rim; iR = inner rim; WM R/C = white matter rim/center; C = center; NAWM = normal-appearing white matter

Fig. 4 Late lesion cell phenotype profiles. **(a)** Marker expression heatmap for the myeloid, astrocyte and T cell phenotypes, identified by PhenoGraph clustering on histoCAT using segmented cells (n = 6698). The heatmap displays relative expression levels based on Z-score normalized marker intensity values, and single cells are hierarchically clustered within each phenotype group. Labels at the bottom of the heatmap indicate the area of the lesion to which each phenotype localizes. **(b)** Violin plot representation of the data in **(a)**. **(c)** t-SNE plot showing the phenotype clusters. Compared to the early lesion, myeloid cell phenotypes show a low degree of separation. **(d)** t-SNE plot colored by marker intensity, confirming the separation of $CD68^+$, $S100B^+$ and $CD3^+$ cell types. R = rim; C = center; PVS = perivascular space; NAWM = normal-appearing white matter

Fig. 5 Late lesion phenotype spatial distributions and transition analyses. **(a)** Spatial organization of myeloid cell phenotypes in the lesion. Phenotypes in the rim (m3), perivascular space (m4) and NAWM (m7) separate into distinct zones, while lesion center phenotypes (m1, m2, m5, m6, m8, m9) are uniformly distributed. **(b)** Spatial distribution of astrocyte phenotypes. One phenotype (a1) predominantly occupies the lesion center and the other (a2) occupies the rim. **(c)** T cells are primarily distributed in the lesion center. **(d)** PHATE mapping of myeloid cells, showing that two lesion center phenotypes (m2, m6) are on a continuum with perivascular space cells (m4, white arrows). **(e)** Pseudotime analysis of myeloid cells shows a similar trajectory to PHATE mapping. Phenotype color schemes on the PHATE and Pseudotime plots reflect the color palettes specific to each analysis. Scale bar for **a-c** = 200 μm. R = rim; C = center; PVS = perivascular space; NAWM = normal-appearing white matter

Fig. 6 Single-cell marker correlations in the late lesion. **(a, b)** Co-expression of Mac2 and MerTK, and LAMP1 and MerTK in **(a)** myeloid cells (n = 6100), and **(b)** astrocytes (n = 528). Co-expression plots are shown with linear expression values and regression lines with Pearson correlation coefficients, and in flow cytometry contour plot form with log10-transformed expression values

Fig. 7 Neighborhood and spatial variance component analyses for the early and late lesions. **(a, b)** Neighborhood analysis heatmaps of all significant pairwise phenotype interactions (red) and avoidances (blue) in the **(a)** early and **(b)** late lesions. White represents no significant spatial relationship. Dark boxes are highly significant spatial relationships ($p < 0.01$). Lightly shaded boxes are less significant relationships ($p < 0.05$) and interactions between cells of the same or spatially adjacent phenotypes. Rows visualize the significance of a phenotype surrounded by other phenotypes, and columns visualize the significance of a phenotype surrounding other phenotypes. **(c, d)** Spatial variance component analysis (SVCA) for the **(c)** early and **(d)** late lesions, showing the proportion of marker expression variance attributable to neighboring cell influences, environmental stimuli, cell-intrinsic factors and residual noise in different lesion zones. Additional plots show the average proportion of marker variance attributable to each factor in different lesion zones. G/WM = gray and white matter; WM = white matter; PVS = perivascular space; NAWM = normal-appearing white matter

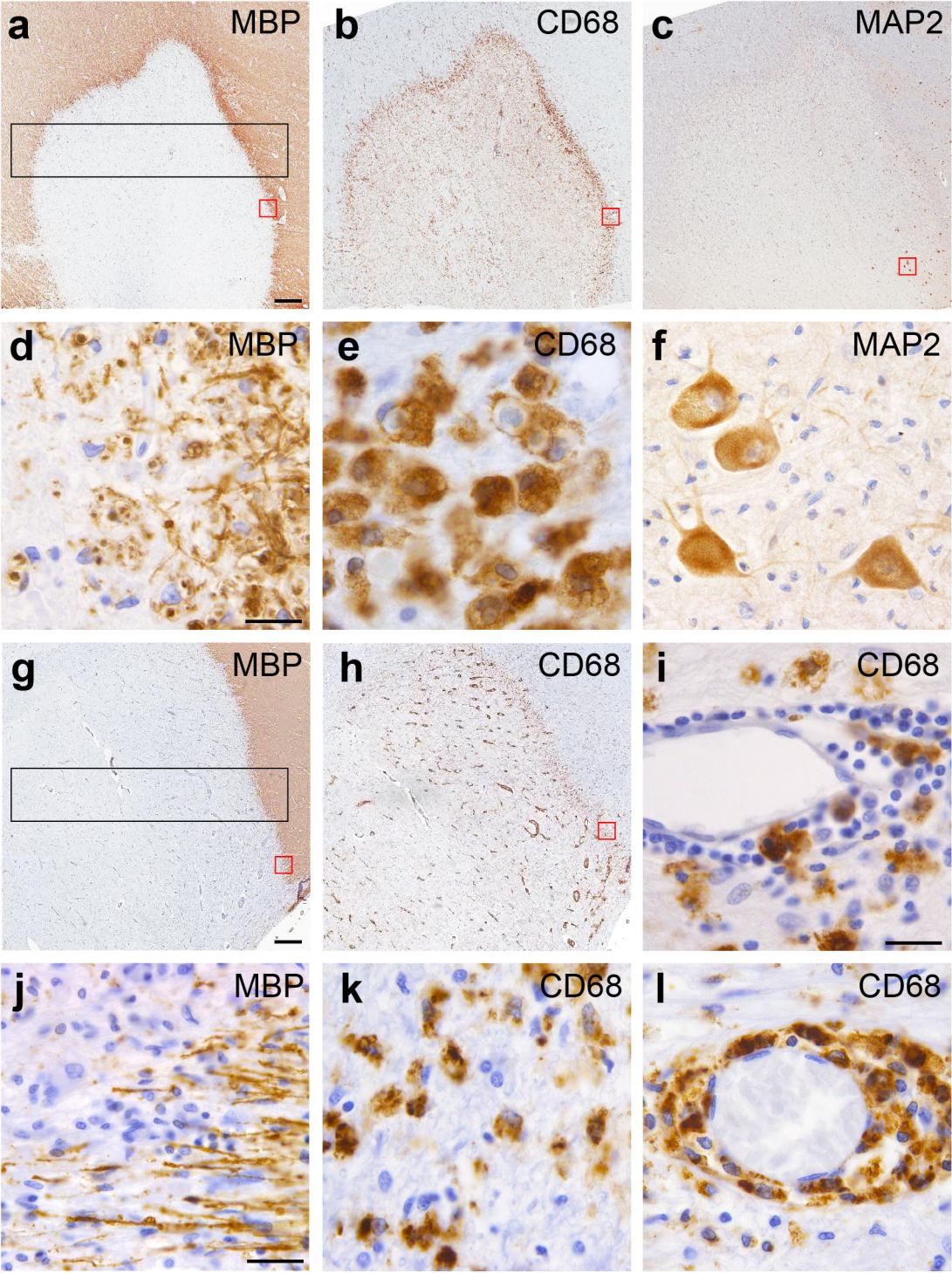
a
MBP
b
CD68
c
MAP2
d
MBP
e
CD68
f
MAP2
g
MBP
h
CD68
i
CD68
j
MBP
k
CD68
l
CD68

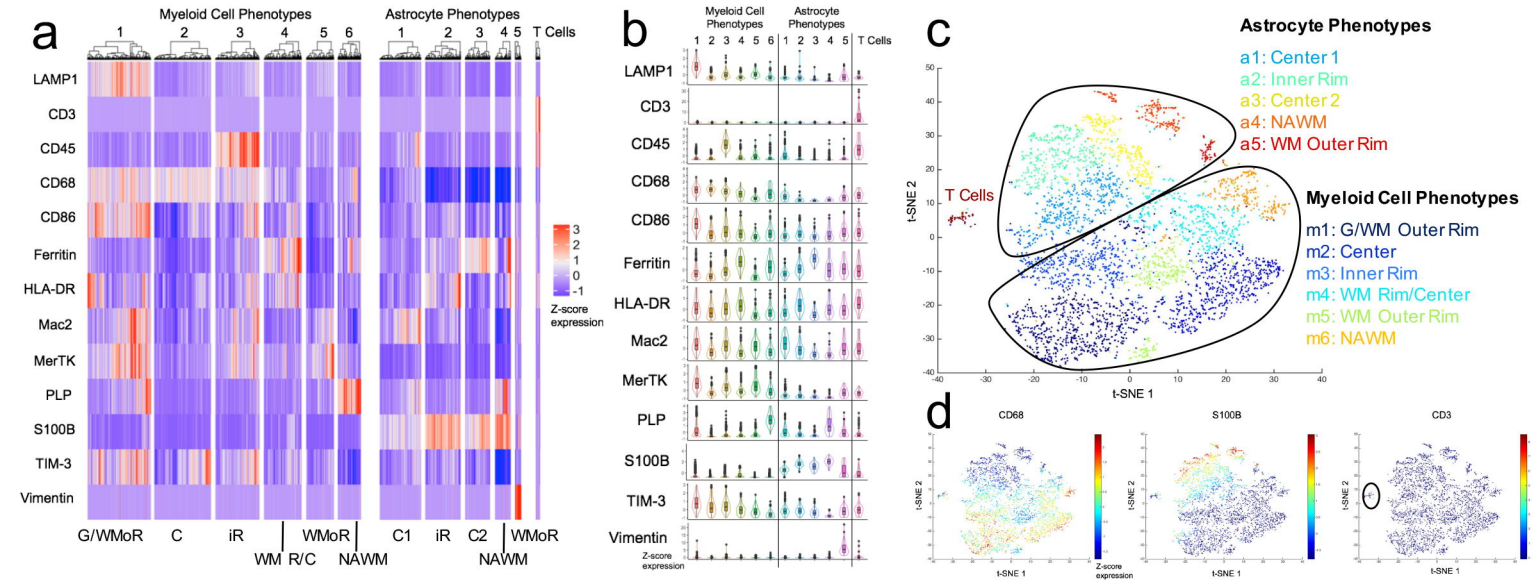
a
Myeloid Cell Phenotypes
Astrocyte Phenotypes
T Cells
LAMP1
CD3
CD45
CD68
CD86
Ferritin
HLA-DR
Mac2
MerTK
PLP
S100B
TIM-3
Vimentin
Z-score expression
G/WMoR
C
iR
WMoR
C1
iR
C2
WMoR
WM R/C
NAWM
NAWM
b
Z-score expression
c
Astrocyte Phenotypes
a1: Center 1
a2: Inner Rim
a3: Center 2
a4: NAWM
a5: WM Outer Rim
T Cells
Myeloid Cell Phenotypes
m1: G/WM Outer Rim
m2: Center
m3: Inner Rim
m4: WM Rim/Center
m5: WM Outer Rim
m6: NAWM
t-SNE 1
t-SNE 2
d
CD68
S100B
CD3
Z-score expression

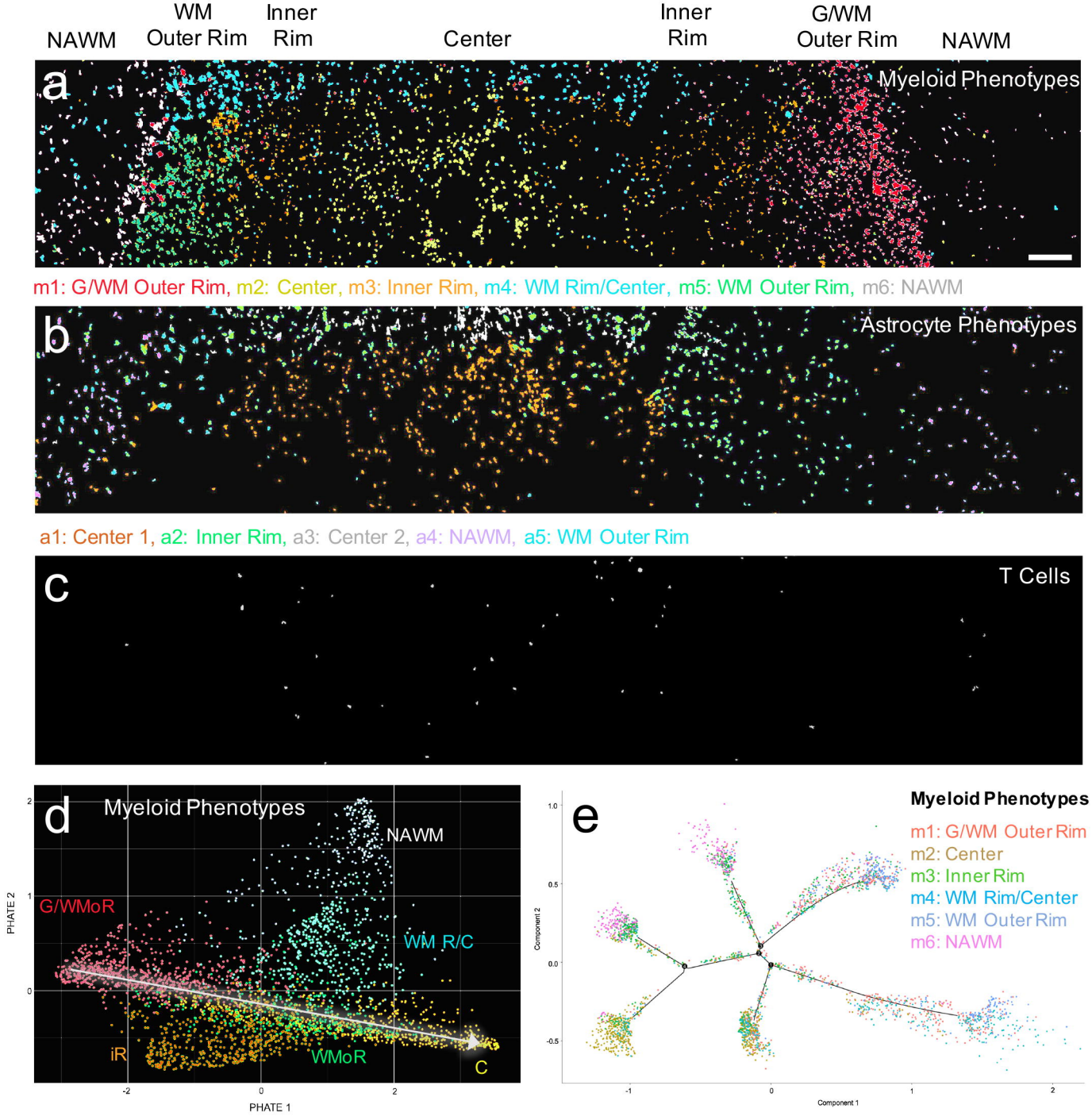
NAWM
WM Outer Rim
Inner Rim
Center
Inner Rim
G/WM Outer Rim
NAWM
a
Myeloid Phenotypes
m1: G/WM Outer Rim, m2: Center, m3: Inner Rim, m4: WM Rim/Center, m5: WM Outer Rim, m6: NAWM
b
Astrocyte Phenotypes
a1: Center 1, a2: Inner Rim, a3: Center 2, a4: NAWM, a5: WM Outer Rim
c
T Cells
d
Myeloid Phenotypes
NAWM
G/WMoR
WM R/C
iR
WMoR
C
PHATE 2
PHATE 1
e
Myeloid Phenotypes
m1: G/WM Outer Rim
m2: Center
m3: Inner Rim
m4: WM Rim/Center
m5: WM Outer Rim
m6: NAWM
Component 2
Component 1

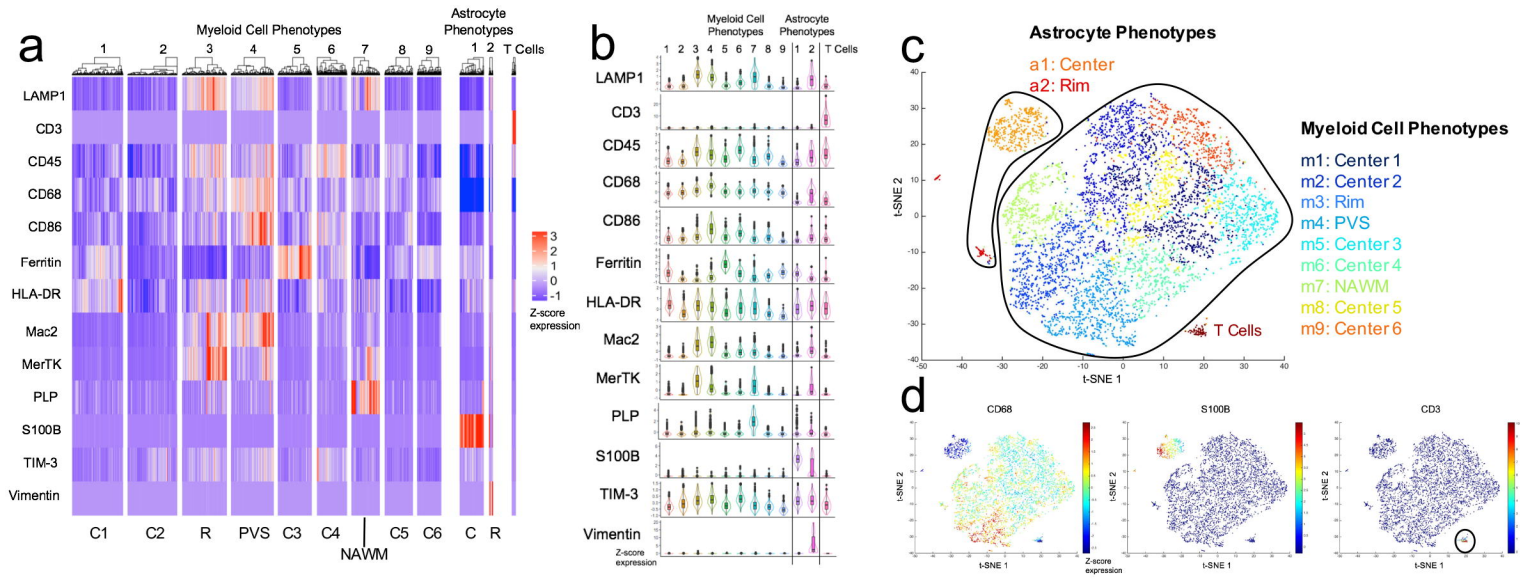
a
Myeloid Cell Phenotypes
Astrocyte Phenotypes
T Cells
LAMP1
CD3
CD45
CD68
CD86
Ferritin
HLA-DR
Mac2
MerTK
PLP
S100B
TIM-3
Vimentin
Z-score expression
C1
C2
R
PVS
C3
C4
NAWM
C5
C6
C
R
b
Myeloid Cell Phenotypes
Astrocyte Phenotypes
T Cells
Z-score expression
c
Astrocyte Phenotypes
a1: Center
a2: Rim
T Cells
t-SNE 1
t-SNE 2
Myeloid Cell Phenotypes
m1: Center 1
m2: Center 2
m3: Rim
m4: PVS
m5: Center 3
m6: Center 4
m7: NAWM
m8: Center 5
m9: Center 6
d
CD68
S100B
CD3
Z-score expression

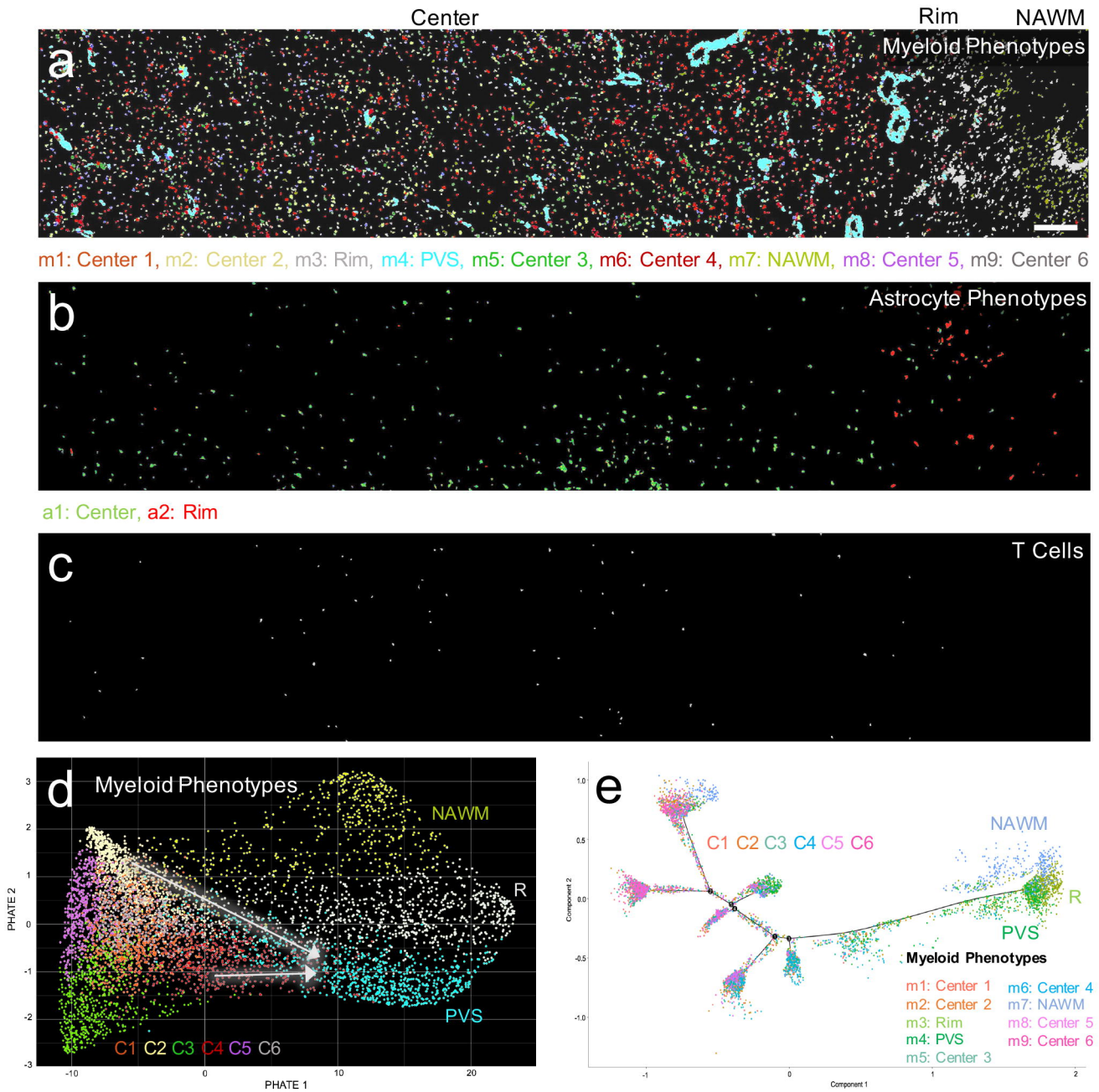
Center
Rim
NAWM
a
Myeloid Phenotypes
m1: Center 1, m2: Center 2, m3: Rim, m4: PVS, m5: Center 3, m6: Center 4, m7: NAWM, m8: Center 5, m9: Center 6
b
Astrocyte Phenotypes
a1: Center, a2: Rim
c
T Cells
d
Myeloid Phenotypes
NAWM
R
PVS
C1 C2 C3 C4 C5 C6
PHATE 2
PHATE 1
e
C1 C2 C3 C4 C5 C6
NAWM
R
PVS
Myeloid Phenotypes
m1: Center 1
m2: Center 2
m3: Rim
m4: PVS
m5: Center 3
m6: Center 4
m7: NAWM
m8: Center 5
m9: Center 6
Component 1
Component 2

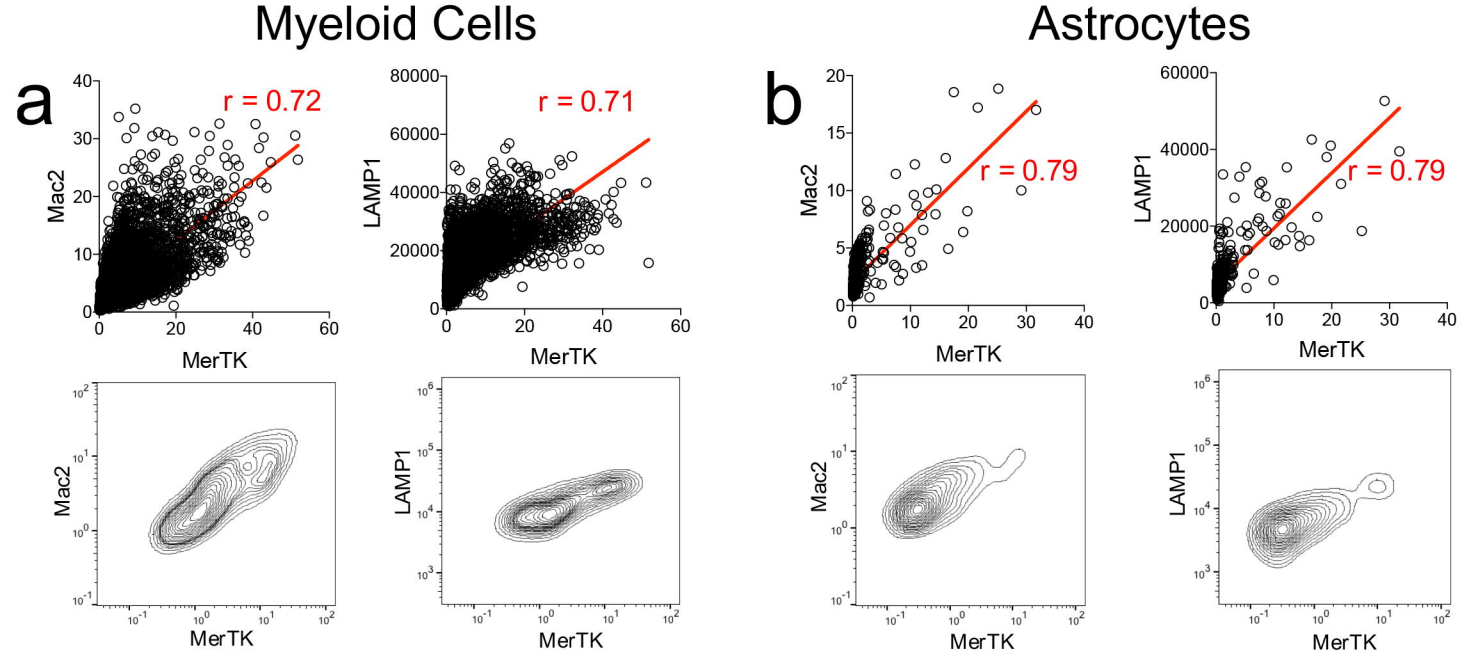
Myeloid Cells
Astrocytes
a
b
r = 0.72
r = 0.71
r = 0.79
r = 0.79
Mac2
LAMP1
MerTK

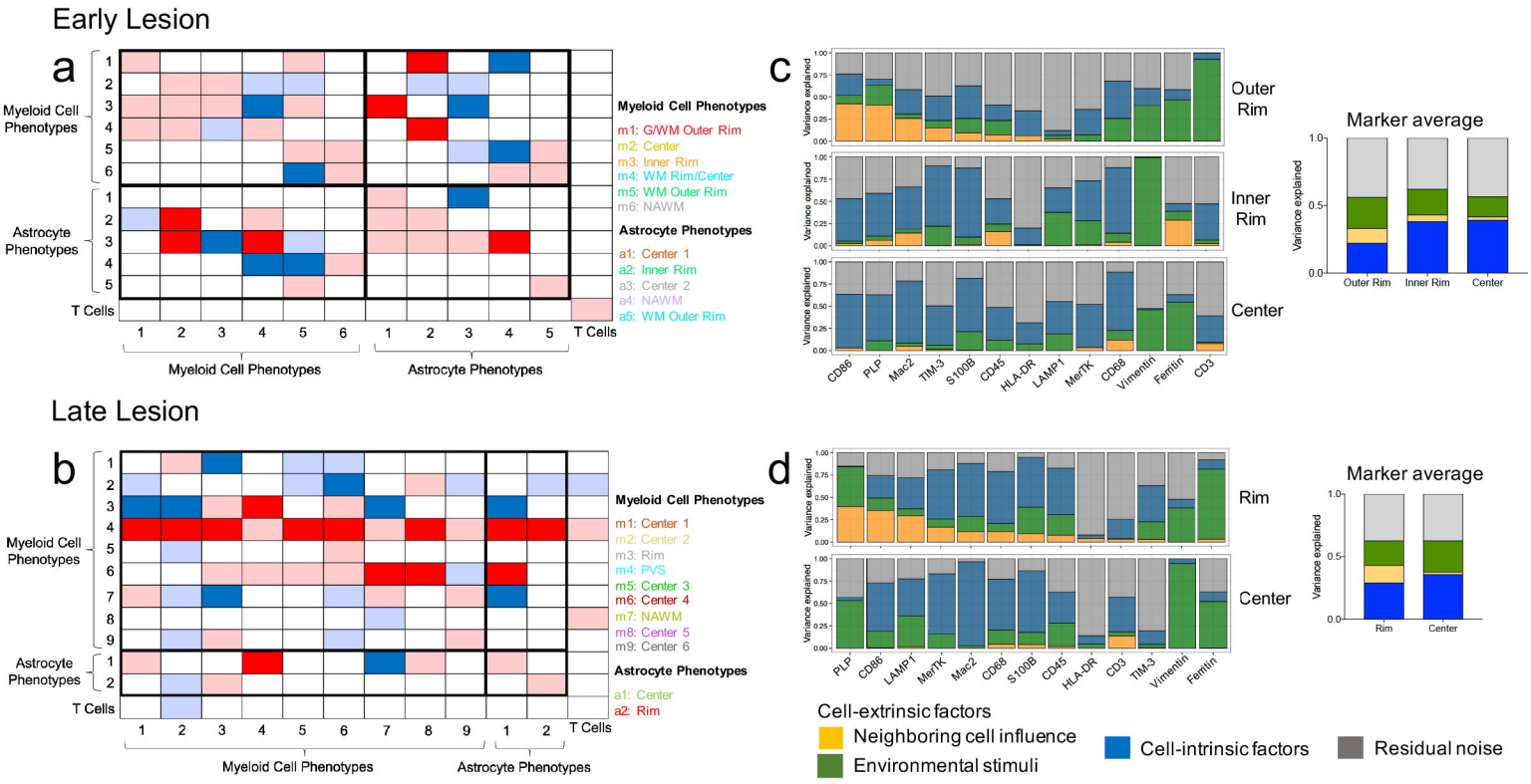
Early Lesion
a
Myeloid Cell Phenotypes
Astrocyte Phenotypes
T Cells
Myeloid Cell Phenotypes
m1: G/WM Outer Rim
m2: Center
m3: Inner Rim
m4: WM Rim/Center
m5: WM Outer Rim
m6: NAWM
Astrocyte Phenotypes
a1: Center 1
a2: Inner Rim
a3: Center 2
a4: NAWM
a5: WM Outer Rim
c
Outer Rim
Inner Rim
Center
Variance explained
CD86
PLP
Mac2
TIM-3
S100B
CD45
HLA-DR
LAMP1
MerTK
CD68
Vimentin
Ferritin
CD3
Marker average
Outer Rim
Inner Rim
Center
Late Lesion
b
Myeloid Cell Phenotypes
m1: Center 1
m2: Center 2
m3: Rim
m4: PVS
m5: Center 3
m6: Center 4
m7: NAWM
m8: Center 5
m9: Center 6
Astrocyte Phenotypes
a1: Center
a2: Rim
d
Rim
Center
PLP
CD86
LAMP1
MerTK
Mac2
CD68
S100B
CD45
HLA-DR
CD3
TIM-3
Vimentin
Ferritin
Marker average
Rim
Center
Cell-extrinsic factors
Neighboring cell influence
Environmental stimuli
Cell-intrinsic factors
Residual noise